Journal of Wind Engineering & Industrial Aerodynamics 181 (2018) 46–60

Contents lists available at ScienceDirect

Journal of Wind Engineering & Industrial Aerodynamics

journal homepage: www.elsevier.com/locate/jweia

Unsteady aerodynamic characteristics of long-span roofs under forced excitation

Tian Li [a,c], Qingshan Yang [b,c,*], Takeshi Ishihara [a]

[a] Department of Civil Engineering, School of Engineering, The University of Tokyo, Tokyo, 113-8656, Japan
[b] School of Civil Engineering, Chongqing University, Chongqing, 400044, China
[c] Beijing's Key Laboratory of Structural Wind Engineering and Urban Wind Environment, Beijing, 100044, China

ARTICLE INFO

Keywords:
Long-span roof
Large eddy simulation
Wind load characteristics
Forced excitation
Unsteady aerodynamic force

ABSTRACT

Wind-induced vibration is significant for light and flexible structures, and aerodynamic effect has to be considered in the estimation of wind load and dynamic response of these structures. The unsteady aerodynamic characteristics of long-span roofs are investigated numerically in this paper using Large Eddy Simulation. Roofs under forced excitation are simulated, and the distributions of aerodynamic coefficients on rigid and vibrating roofs are estimated. The computed coefficients show good agreement with the experimental results. The influences of inflow turbulence, shape of roof and other parameters on the aerodynamic coefficients are also analyzed. It is found that the mean wind pressure coefficients mainly depend on the vortex shedding and reattachment positions. These coefficients in the cases studied remain almost the same with increasing excitation frequency, while the fluctuating pressure coefficients and unsteady aerodynamic coefficients change with frequency regularly. The probability density functions of wind pressure on the vibrating roofs show obvious non-Gaussian characteristics, and the wind pressure spectra exhibit peaks at the excitation frequencies. The dynamic response of long-span roof is then predicted using the mechanical admittance function. Results show that the displacement response of the structure will be under-estimated without considering the unsteady aerodynamic effect especially for flexible structures.

1. Introduction

Long-span roofs have been widely used in recent years in stadium halls, theaters, conference and exhibition centers, airport terminals and other large-scale buildings. These structures are very sensitive to wind load because of their lightweight and flexibility. The wind field around structures changes under strong wind leading to distinct characteristics of wind load on the structures. This phenomenon is called the Fluid-Structure Interaction (FSI) (Shen and Wu, 2002). Structures may absorb energy from wind because of the FSI effect under certain conditions, e.g. at certain ranges of wind velocity. The vibration amplitude of structures will increase greatly with possible aero-elastic instability phenomena (Sharekh and Pathak, 2000). Several large flexible roof structures have collapsed in the last several decades under wind actions, e.g. the roof of Kumamoto Park Dome, in Japan 1999, the top of Jeju World Cup Stadium, in Korea 2002, the roof of Pinghu Stadium, in China 2012, etc. (Chen, 2015). It is worth mentioning that these accidents occurred under wind velocities lower than the design values. Most of wind-induced vibration analyses of long-span flexible roofs are based on wind tunnel tests of rigid models where the FSI effect has not been considered. This may lead to an under-estimation of the wind effect on flexible structures under strong wind resulting in potential hazards (Yang et al., 2010).

Theoretical analysis has been applied to study the FSI effect and aero-elastic instability of long-span structures. The dynamic equations of fluid and structure can be simplified based on assumptions. The critical condition for aero-elastic structural instability is always obtained from methods like eigenvalue analysis. Kunieda (1975) presented a method to determine the critical flutter wind velocity of two-dimensional hanging roofs and curved membrane roofs. The governing equations were derived based on classical flow theory with the vortex in the boundary layer and the flow separation around structure neglected. Kimoto and Kawamura (1983) derived the dynamic equation of a one-way suspended roof in uniform flow with the modified thin-wing theory and the revised Kutta-Joukowski condition. They proposed the criterion on the wind velocity of aero-elastic instability by using the conservation principle of

* Corresponding author. School of Civil Engineering, Chongqing University, Chongqing, 400044, China.
E-mail address: qshyang@cqu.edu.cn (Q. Yang).

https://doi.org/10.1016/j.jweia.2018.08.005
Received 27 February 2018; Received in revised form 7 August 2018; Accepted 7 August 2018

potential energy. Yang and Liu (2005) derived theoretical equations for calculating the additional mass and aerodynamic damping based on the simplified potential fluid theory. They also presented an analytical formula for the critical wind velocity of wind-induced instability for a three-dimensional roof, where the effect of negative aerodynamic damping could be considered by combining the non-moment theory of thin shells and the potential fluid theory. However, the above theoretical studies do not include turbulent inflow conditions and bluff body aerodynamic effects despite their importance (Tamura and Kareem, 2013).

Wind tunnel experiment of aero-elastic model is one of the common methods to identify the unsteady aerodynamic coefficients of long-span roofs. The previous experimental studies are mainly on one-way roofs which can be simplified as two-dimensional problems and are sensitive to wind due to their poor stabilities. These studies show that the roofs will resonate under vortex shedding at certain wind velocities. The unstable vibration mode of roof is the first-order asymmetric mode with the vibration amplitude limited rather than divergent. This phenomenon is called “lock-in”. Matsumoto (1990) found that the first-order asymmetric mode of the roof would be self-excited, because the frequency of vortex separated at the leading edge of the roof was coupled with the frequency of the first-order asymmetric mode of the roof. Miyake et al. (1992) showed that the Karman vortex shedding around roofs is the main cause of wind-induced vibration. Chen et al. (2015) carried out a wind tunnel test for a closed type one-way tensioned membrane structure in a uniform flow. The frequency of vortex shedding at low wind velocity was found much lower than the structural natural frequency. When the wind velocity increased and vortex shed at a frequency close to the structural frequency of the first asymmetric mode, the structure would be forced to vibrate and the phenomenon of lock-in occurred. Although the displacement characteristics of the roof can be identified from experiments with the aero-elastic model, yet the wind load test is not easy to conduct with the lightweight and flexibility of the long-span roof model. The test results are also influenced by the presence of the pressure sensors resulting in unsatisfactory similarity conditions on the material properties.

Since most evidences (Matsumoto, 1990; Chen et al., 2015) show that the one-way long-span roof vibrates in the first order asymmetric mode under wind action with limited vibration amplitudes, forced vibration test has been popularly used to obtain the unsteady aerodynamic forces instead of the aero-elastic model test. Daw and Davenport (1989) obtained the aerodynamic forces on a semi-circular roof based on forced vibration experiment, and they commented that the aerodynamic forces depended on the inflow velocity, vibration frequency and amplitude whereas they had little relationship with the inflow turbulence and the Reynolds number. Ohkuma and Marukawa (1990) showed that with increasing vibration frequency and amplitude, the aerodynamic stiffness coefficient of long-span flat roofs would increase, and the aerodynamic damping coefficient would decrease from positive to negative. Kawai et al. (1999) studied the aerodynamic properties of a large cantilevered roof using forced vibration experiments, and they found that the frequency of the sharp peak in the wind pressure spectrum was the natural frequency of the roof lowered by the positive aerodynamic stiffness coefficients. The lowered natural frequency synchronized with the frequency of vortex shedding at the leading edge of the roof, and this caused negative damping coefficients.

There are, however, limitations in the forced excitation experiments. The excitation system is complicated, and higher vibration modes of the roof model are difficult to obtain (Daw and Davenport, 1989). This kind of test can only be used to obtain simple vibration modes with small vibration amplitudes, whereas Computational Fluid Dynamic (CFD) analysis performs better for complicated vibration modes and large vibration amplitudes. Oka and Ishihara (2009) investigated the unsteady aerodynamic characteristics of a square prism in a uniform flow at various angles of attack using Large Eddy Simulation (LES) turbulence model. The numerical results of mean aerodynamic coefficients, surface pressures, and flow patterns for all angles of attack had good match to the experimental results. Ding et al. (2014) studied the unsteady aerodynamic force coefficients of long-span curved roof using LES model also with good results. Nevertheless, the numerical study on the unsteady aerodynamic characteristics of long-span roofs is still limited so far. Accurate numerical prediction of aerodynamic forces on the flat roof with strong flow separation is a challenge. The aerodynamic mechanism of the vibrating roof is also not fully understood. The influences of roof shape, inflow turbulence and vibrating condition on the aerodynamic phenomena need to be studied further. The LES turbulence model has been shown an exhibit superior performance in the simulation of strong separation flows near structures and the precise prediction of wind load on the surface of structure (Ferziger and Peric, 2002). Therefore, three-dimensional LES is used in this paper to simulate a flat and a curved roof with turbulent inflows. The predicted wind pressure coefficients and unsteady aerodynamic force coefficients are compared with experimental results for the validation of the numerical method. The unsteady aerodynamic characteristics and behavior of long-span roofs are analyzed with the wind load coefficients and the flow patterns. The dynamic response of flexible roof is finally obtained with consideration of the unsteady aerodynamic effect.

2. Numerical model and parameters for the studies

2.1. Governing equations

In the following LES analysis, large eddies are directly computed in simulations, while the influence of eddies smaller than the control volume are parameterized. The governing equations for the LES analysis are derived by filtering the continuity and Navier-stokes equations as

$$\frac{\partial \rho \tilde{u}_i}{\partial x_i} = 0 \tag{1}$$

$$\frac{\partial}{\partial t}(\rho \tilde{u}_i) + \frac{\partial}{\partial x_j}(\rho \tilde{u}_i \tilde{u}_j) = \frac{\partial}{\partial x_j}\left(\mu \frac{\partial \tilde{u}_i}{\partial x_j}\right) - \frac{\partial \tilde{p}}{\partial x_i} - \frac{\partial \tau_{ij}}{\partial x_j} \tag{2}$$

where x_i and x_j are the coordinates. The subscript i and j stand for different directions in Cartesian coordinates include streamwise, spanwise and vertical directions, and t is time instant. The $\sim$ denotes the filtered component; $\tilde{u}$ and $\tilde{p}$ are filtered velocity and filtered pressure respectively. μ and ρ are the viscosity and density of air respectively, and τ_{ij} is the subgrid-scale stress defined by

$$\tau_{ij} = \rho \tilde{u}_i \tilde{u}_j - \rho \widetilde{u_i u_j} \tag{3}$$

The subgrid-scale stresses resulting from the filtering operations are unknown, and they are modelled as

$$\tau_{ij} = -2\mu_t \tilde{S}_{ij} + \frac{1}{3}\tau_{kk}\delta_{ij} \tag{4}$$

where μ_t is the subgrid-scale turbulent viscosity, and δ_{ij} is the Kronecker delta. $\tilde{S}_{ij}$ is the rate-of-strain tensor for the resolved scale defined as

$$\tilde{S}_{ij} = \frac{1}{2}\left(\frac{\partial \tilde{u}_i}{\partial x_j} + \frac{\partial \tilde{u}_j}{\partial x_i}\right) \tag{5}$$

Smagorinsky model (Smagorinsky, 1963) is adopted to model the subgrid-scale turbulent viscosity, μ_t, as

$$\mu_t = \rho L_s^2 |\tilde{S}| = \rho L_s^2 \sqrt{2\tilde{S}_{ij}\tilde{S}_{ij}} \tag{6}$$

where $|\tilde{S}| = \sqrt{2\tilde{S}_{ij}\tilde{S}_{ij}}$ and L_s is the mixing length of subgrid-scales defined as

$$L_s = \min(\kappa d, C_s V^{1/3}) \tag{7}$$

Table 1
Details of reference works.

	Roof shape	Method	Re number $\rho UH/\mu$	Inflow condition	Mean roof height H (cm)	Vibration amplitude z_0	Vibration frequency f_m
Ohkuma and Marukawa (1990)	flat	experiment	2.5×10^4	Uniform turbulence	6	1.7%-10%H	5–50 Hz
Ding et al. (2014)	curved	experiment and CFD	2.7×10^4	ABL	8	5%H	5–25 Hz (exp.) 10–160 Hz (CFD)

Note: U denotes the mean wind velocity at the mean roof height H. ABL stands for the atmospheric boundary layer flow.

where κ is the von Karman constant and is taken equal to 0.42. C_s is Smagorinsky constant. d is the distance to the closest wall, and V is the volume of a computational cell.

In general, $C_s = 0.1$ is widely used in the simulation with finite volume/difference methods (Ferziger and Peric, 2002). Most of them employ explicit discretization scheme for the unsteady term in which negative numerical diffusion is inherently contained. On the other hand, numerical schemes with few diffusions such as spectrum method use small C_s values. In this study, the second order implicit discretization scheme is utilized, in which the numerical diffusions are few and positive. Ma et al. (2000) conducted a systematic study on the flow around a circular cylinder. The aerodynamic coefficients obtained by using $C_s = 0.032$ are closest to those obtained by the spectrum method. This value is adopted for all the studies in this report.

When a wall-adjacent cell is in the laminar sub-layer, the wall shear stress is obtained from the laminar stress-strain relationship as

$$\frac{\tilde{u}}{u_\tau} = \frac{\rho u_\tau \bar{y}}{\mu} \tag{8}$$

where $\tilde{u}$ is the filtered velocity that is tangential to the wall; u_τ is the friction velocity; $\bar{y}$ is the distance between the center of the cell and the wall. If the mesh cannot resolve the laminar sub-layer, it is assumed that the centroid of the wall-adjacent cells falls within the logarithmic region of the boundary layer, and the law-of-the-wall is employed as

$$\frac{\tilde{u}}{u_\tau} = \frac{1}{\kappa} \ln E\left(\frac{\rho u_\tau \bar{y}}{\mu}\right) \tag{9}$$

where the constant E is taken equal to 9.8.

2.2. Reference experiments

The experimental and numerical results by Ohkuma and Marukawa (1990) and Ding et al. (2014) serve as reference for validation of the proposed method, and details of them are summarized in Table 1. The model sizes, span/height ratios and the Reynolds numbers in these two cases are similar. The reference studies have been conducted under well-controlled laboratory conditions with turbulent inflows, high Reynolds numbers (>10000) and low blocking rates (<5%). Other parameters like inflow profiles, mean and fluctuating pressure coefficients and unsteady aerodynamic forces can also be found in the above references.

The displacement of the roof $\bar{z}_j$ under forced vibration is of the first anti-symmetric mode given as

$$\bar{z}_j(s,t) = \varphi_j(s)\bar{x}_j(t) \tag{10}$$

$$\varphi(s)_{j=1} = \sin 2\pi \frac{s}{R_s} \tag{11}$$

$$\bar{x}_j(t) = z_0 \sin(2\pi f_m t) \tag{12}$$

where φ_j and $\bar{x}_j$ are respectively the mode function and generalized displacement in the jth mode; s denotes the distance from the leading edge of roof and R_s is the total length of the roof; z_0 and f_m are the amplitude and frequency of forced excitation respectively. These shape parameters of the roof model and the vibration mode are shown in Figs. 1 and 2 respectively.

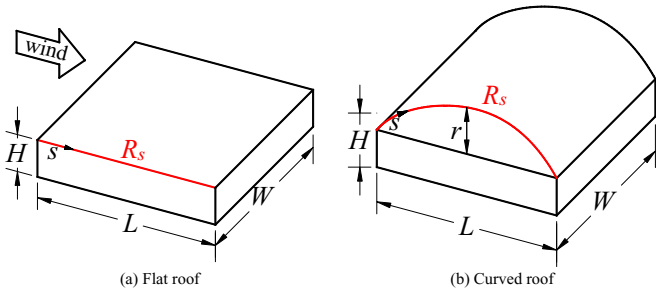

Fig. 1. Geometry of roof model.

2.3. Numerical model

The calculation domain and mesh configuration of the numerical model are shown in Figs. 3 and 4 respectively. The dimensions of the flat roof are 0.36 m × 0.4 m × 0.06 m ($L \times W \times H$), where L, W and H represent the length, width and eaves height of the flat roof above ground respectively. Uniform turbulent inflow of 7% turbulence intensity is generated by grid as shown in Fig. 3(a), same as that in the experiment of Ohkuma and Marukawa (1990). The dimensions of the curved roof are 0.4 m × 0.24 m × 0.08 m ($L \times W \times H$) with the rise/span ratio $r/L = 0.15$, where H represent the mean height of the curved roof. The inflow is the atmospheric boundary layer turbulence flow generated by spires and roughness blocks as shown in Fig. 3(b), similar to that in the experiment of Ding et al. (2014). Both Fig. 4(a) and (b) show the refined mesh at roof corners with 60 nodes in the roof height direction. Mesh interval size in the width direction is 3W/20. The corner of the flat roof is modified into a curve as shown in Fig. 4(c). The curve diameter is H/100 and a mesh with small cells is generated near each corner to avoid singularity of the solutions, similar as Sarwar and Ishihara (2010). Such small roundness ratio does not significantly affect the flow characteristics. Fig. 4(d) is the unstructured mesh around grid adopted to generate the uniform turbulent inflow. The wind field mesh around the spires in Fig. 3(b) is also unstructured similar to Fig. 4(d), and is omitted here.

The mesh independency of the solution has been checked with meshes of different refinements. The final mesh at convergence of the numerical results with further refinement is used for all subsequent analyses in this paper. Results show that the first mesh size normal to the wall, Δy, should be small enough and the value of Δy^+, the step of non-dimensional viscous length scale defined as Eq. (13), should be less than or equal to unity to simulate the separated vortices.

$$\Delta y^+ = \frac{\rho u_\tau \Delta y}{\mu} \tag{13}$$

The dependency of time step dt is also checked. The final non-dimensional time step dtU/H at convergence of numerical results with smaller time step is used in subsequent analyses. The aerodynamic parameters are calculated for the duration of $tU/H = 1000$. Results of the

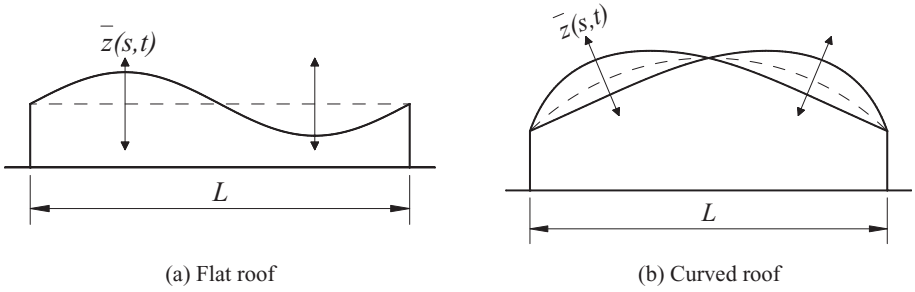

Fig. 2. Vibration mode (First anti-symmetric mode).

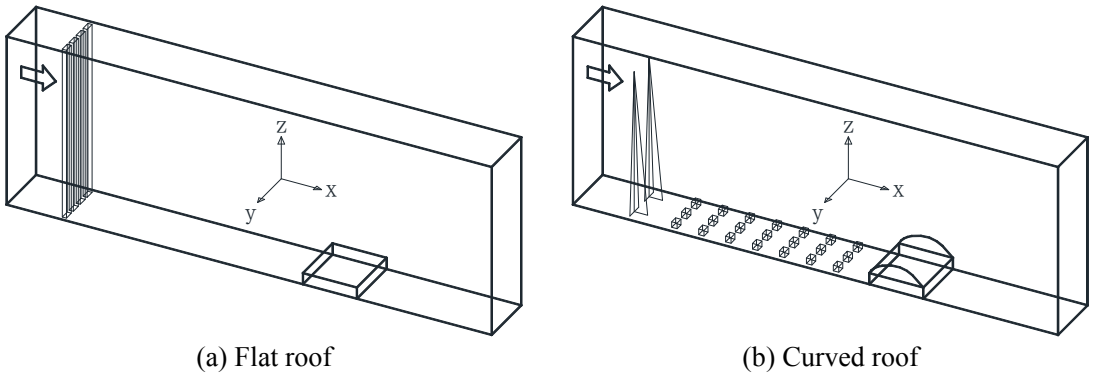

Fig. 3. Computational domain.

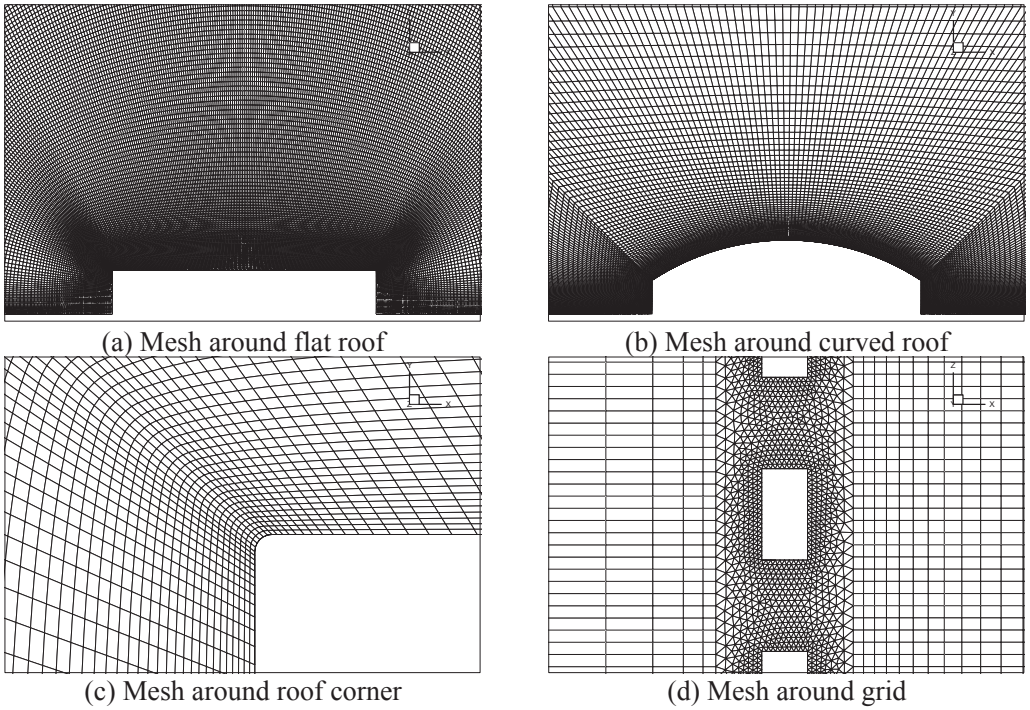

Fig. 4. Mesh arrangement.

initial $tU/H = 400$ time duration are ignored to remove the influence of end effect of data. The final mesh and calculation parameters are shown in Table 2.

The ground and structure surfaces are set as no-slip walls in this research. Uniform velocity condition is specified at the inlet boundary, and zero diffusive condition is adopted at the outlet boundary. Symmetry condition is given for the upper boundary. The side boundary is generally taken as symmetry boundary to reduce the boundary effect of the model at the center of computational domain. However, sectional model is used in this study to minimize the numerical mesh and computational effort, i.e. the width of the roof model is taken the same as that of the whole computational domain. Large fluctuation of inflow turbulence and aerodynamic force are expected in the cross-wind direction for sectional model with symmetric side boundary. Periodic side boundary condition

Table 2
Parameters of numerical model.

	Flat($r/L = 0$)	Curved($r/L = 0.15$)
Mean wind velocity U	6 m/s	5 m/s
Turbulent intensity Iu	7%	19%@H
Excitation amplitude z_0	0.05H	0.05H
Excitation frequency f_m	10–50 Hz	10–50 Hz
Computational domain	12 m(x) × 0.4 m(y) × 2 m(z)	12 m(x) × 0.24 m(y) × 2 m(z)
Roof size	0.36 m(x) × 0.4 m(y) × 0.06 m(z)	0.4 m(x) × 0.24 m(y) × 0.08 m(z)
Mesh of roof	230(x) × 60(y) × 60(z)	120(x) × 36(y) × 60(z)
The number of total mesh	5.68×10^6	2.42×10^6
Non-dimensional time step size (dtU/H) of steady case	0.02	0.02
Non-dimensional time step size (dtU/H) of unsteady case	0.005	0.005

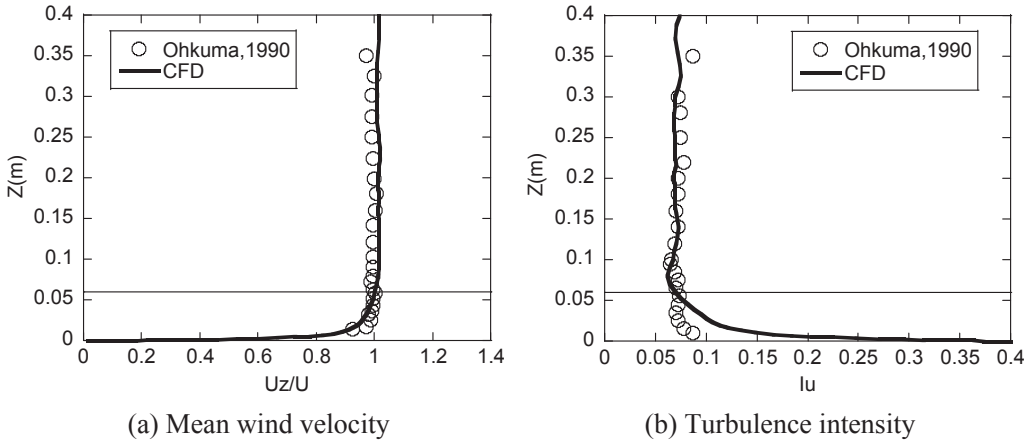

Fig. 5. Wind profile of uniform turbulence flow.

is found to reduce such fluctuation efficiently (Hirsch, 2007), therefore it is adopted in the subsequent analyses of this report.

2.4. Dynamic mesh

Diffusion-based smoothing method is used to update the volume mesh in the roof region subject to the motion defined at the boundaries. This is accomplished by a User Defined Function (UDF) in ANSYS Fluent. When smoothing method is used to adjust the mesh of a zone with a moving and/or deforming boundary, the interior nodes of the mesh move, but the number of nodes and their connectivity does not change. In this way, the interior nodes "absorb" the movement of the boundary. This mesh motion is governed by the diffusion equation (ANSYS Inc., 2015),

$$\nabla \cdot (\gamma \nabla \overline{u}) = 0 \tag{14}$$

where $\overline{u}$ is the mesh displacement velocity. γ is the diffusion coefficient defined as a function of the cell volume with the following form:

$$\gamma = \frac{1}{\overline{V}^{\alpha}} \tag{15}$$

where $\overline{V}$ is the normalized cell volume. Diffusion Parameter $\alpha = 1.0$ denotes that larger cells absorb more motion than the smaller cells and therefore the quality of smaller cells is well preserved.

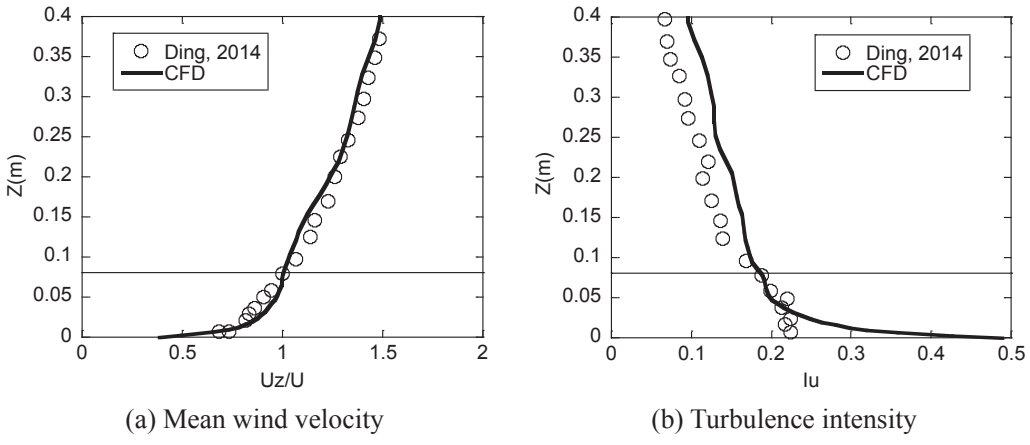

Fig. 6. Wind profile of atmosphere boundary layer flow.

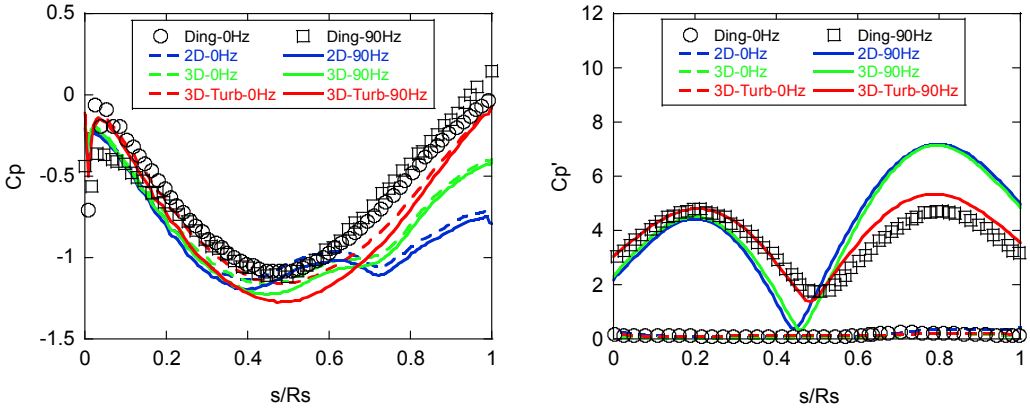

(a) Mean pressure coefficients (b) Fluctuating pressure coefficients

Fig. 7. Wind pressure coefficients with different dimensionalities and inflow conditions.

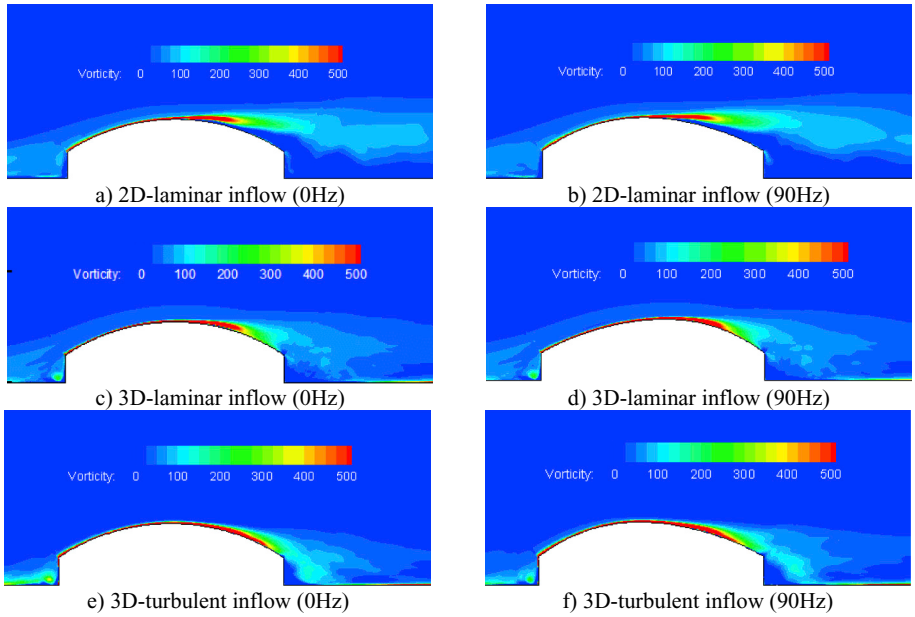

a) 2D-laminar inflow (0Hz) b) 2D-laminar inflow (90Hz)

c) 3D-laminar inflow (0Hz) d) 3D-laminar inflow (90Hz)

e) 3D-turbulent inflow (0Hz) f) 3D-turbulent inflow (90Hz)

Fig. 8. Mean vorticity contours with different dimensionalities and inflow conditions.

2.5. Solution scheme and solution procedure

The 3D unsteady LES filtered Navier-Stokes equations are solved with the commercial CFD code ANSYS Fluent 16.2 (ANSYS Inc., 2015) using the control volume method. The second-order central difference scheme is used for the convective and viscosity terms, and the second-order implicit scheme is used for the unsteady term. SIMPLE (semi-implicit pressure linked equations) algorithm is employed for solving the discritized equations (Ferziger and Peric, 2002).

3. Verification of numerical results

The wind fields around structures are always turbulent and this condition is highly influential to the aerodynamic phenomenon. Grid is used to generate the uniform turbulent inflow in the numerical simulation of the flat roof, and spires and roughness blocks are used to generate the atmospheric boundary layer turbulence for the curved roof as previously stated. These conditions are the same as the reference experiments (Ohkuma and Marukawa, 1990; Ding et al., 2014). The wind profiles are shown in Figs. 5 and 6 with the mean roof heights shown as transverse solid lines and mean wind velocity donated as U_z. The numerical wind velocity and turbulence intensity profiles are noted basically consistent with those in the reference experiments with the relative errors less than 10% near the roof height.

Two-dimensional results with laminar inflow and three-dimensional results with laminar and turbulent inflow are shown in Fig. 7 for the discussion on the influence of calculation domain dimension and inflow turbulence. The wind pressure coefficient $C_p(t)$ is defined as:

$$C_p(t) = \frac{p(t) - p_{ref}}{q_H} \tag{16}$$

where p_{ref} is the reference pressure near outlet; $q_H = \rho U^2/2$ represents the dynamic pressure at the roof height. The mean and standard deviation of the wind pressure coefficient are the mean wind pressure coefficient C_p and fluctuating wind pressure coefficient $C_p^{'}$ respectively. Results for rigid curved roofs and curved roofs vibrating at $f_m = 90$ Hz are studied since the difference of numerical results under different calculation conditions are distinct at high vibration frequency. These results are compared with the numerical results of Ding et al. (2014) with 3D

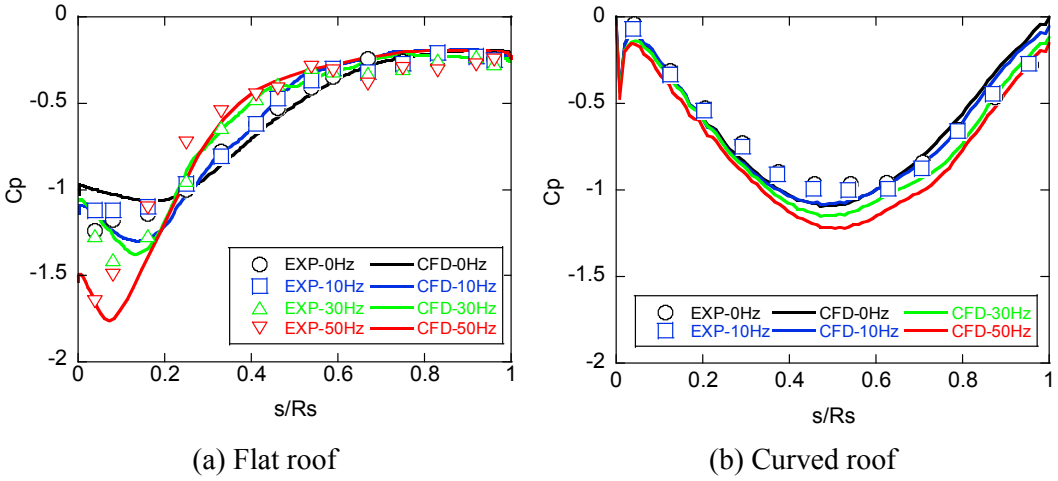

Fig. 9. Mean pressure coefficients of roofs with different vibration frequencies.

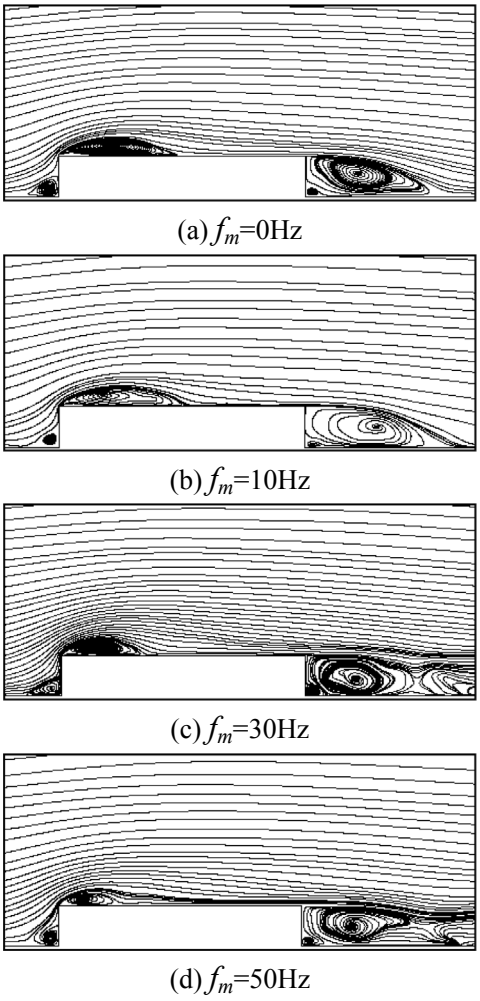

Fig. 10. Mean streamline around flat roof with different vibration frequencies.

calculation and turbulent inflow. Fig. 8 shows the time averaged vorticity contours which help to explain the behavior of the distributions of pressure coefficients.

It is noted that for the same simulation condition, the mean wind pressure coefficients change slightly no matter the roof vibrates or not (Fig. 7(a)). The corresponding mean flow fields for the rigid and vibrating roofs in each condition are similar. However, the results of different simulation conditions are distinct. The mean pressure coefficients of the 2D roof with laminar inflow exhibit two peaks, located in the middle of the roof and $s/R_s = 0.7$. The first peak is caused by the acceleration of wind, and the second one is due to the flow separation, as shown in Fig. 8(a) and (b). For the simulation of 3D domain with laminar inflow, the second peak becomes smaller compared with the 2D results because the vortex intensity decreases from 2D to 3D together with the intensity of wind suction (Fig. 8(c) and (d)). Additionally, the mean pressure coefficients of the 3D roof with turbulent inflow exhibit only one peak near the middle of roof. It can be understood that the inflow turbulence causes an early transition of the boundary layer on the roof surface from laminar to turbulent. Thus the boundary layer is able to withstand better the adverse pressure gradient with turbulent inflow, and the flow separating position moves towards the trailing edge as shown in Fig. 8(e) and (f) such that the second peak caused by the wind separation does not exist.

The fluctuating wind pressure coefficients are low on the rigid roof, but they increase dramatically on the vibrating roof (Fig. 7(b)). The distributions of fluctuating wind pressure coefficients are consistent with the vibration mode, with larger coefficients at positions with larger vibrating amplitude, and the peak values appear near the positions at $s/R_s = 1/4$ and 3/4. For the coefficients of both 2D and 3D simulations with laminar inflow, the first peak is smaller than the second one due to the influence of the separated vortex. As for the 3D simulations with turbulent inflow, the distribution of fluctuating pressure coefficients changes into a nearly symmetric pattern. The simulated results in 3D domain with turbulent inflow coincide with the reference set of results (Ding et al., 2014) which validates the proposed numerical method.

4. Characteristics of wind pressure on roofs

4.1. Mean pressure coefficients

The distributions of mean pressure coefficients on the flat roof and the curved roof with different excitation frequencies are shown in Fig. 9 together with experimental results (Ohkuma and Marukawa, 1990; Ding et al., 2014). The flow pattern of the flat roof in Fig. 10 shows that the flow separates at the leading edge of the flat roof, and it reattaches near the middle part of the roof. A separation bubble appears between the separation and reattachment points. The mean pressure coefficient reaches its biggest negative value near the separation point, and then

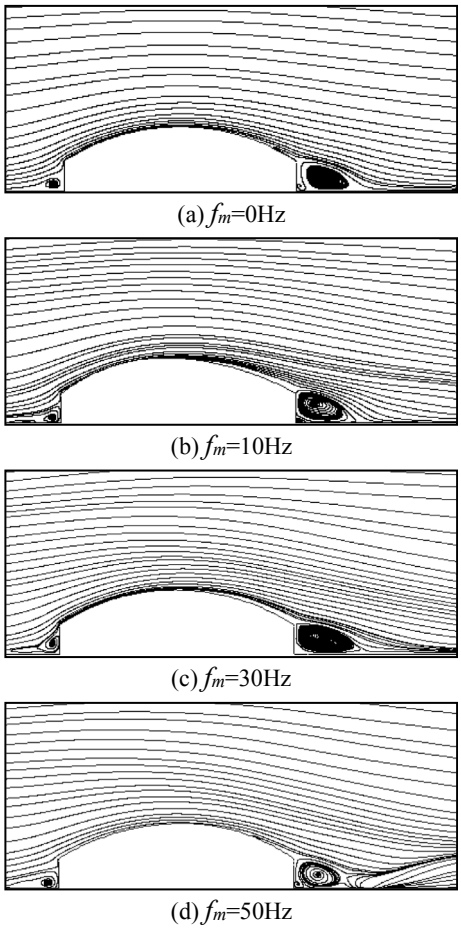

Fig. 11. Mean streamline around curved roof with different vibration frequencies.

decreases to a relatively stable value behind the reattachment point (Fig. 9(a)). With increasing vibration frequency, the separating position does not change while the reattaching position moves towards the leading edge. Meanwhile, the vortex intensity increases according to the mean vorticity contours which are omitted here. Consequently, the peak value of negative mean pressure coefficients increases and moves towards the leading edge of the flat roof.

The distributions of mean pressure coefficients on the curved roof are quite different from those on the flat roof as shown in Fig. 9(b). The negative mean pressure appears mainly due to the acceleration of flow above the roof. The vortex sheds near the trailing edge with turbulent inflow no matter the roof vibrates or not, as shown in Fig. 11. Meanwhile, the size of vortex behind the vibrating roof remains the same as the static one, resulting in similar mean wind pressure distributions with different vibration frequencies.

4.2. Fluctuating pressure coefficients

The fluctuating pressure coefficients are shown in Fig. 12. The fluctuating pressure coefficients on rigid roofs are small, which are mainly caused by the turbulence of inflow and wake, while the coefficients on vibrating roofs are induced by vibration as well, which increase with excitation frequency. The distribution of fluctuating pressure coefficients for high vibration frequencies are consistent with vibration mode. Large coefficients appear at positions with large vibration amplitudes and vice versa. Although the fluctuating pressure components of the inflow and wake turbulence are different for roofs with different shapes, yet their fluctuating pressure distributions are similar for the same vibration mode.

The characteristics of the fluctuating wind pressure are further studied similar to that for the mean wind pressure. The transient vorticity around the roofs obtained from numerical simulation are shown in Figs. 13 and 14, where φ donates the phase in a vibration cycle and the vibration frequency is 50 Hz as an example. It is noted that the flow separates at the leading edge of the flat roof, and the separated flow contains vortices of different scales. The large scale vortex is further separated into smaller ones along the downstream direction, and they finally dissipate. These vortices in the front part of the flat roof is relatively dense with high strength, so that the fluctuating wind pressure is not exactly consistent with the vibration mode in this part. However, the fluctuating wind pressure in the leeward part of the roof is mainly due to the vibration of structure, so that its distribution and vibration mode are consistent. For the curved roofs, the vortices fall off near the trailing edge of the roof, which have less influence on the flow field above the roof. The fluctuating wind pressure distribution coincides with the vibration mode as a result.

4.3. Non-Gaussian characteristics of wind pressure

The wind pressures in engineering studies are usually assumed to be Gaussian. This assumption is, however, not true for the vibrating structures where the wind pressures are generally non-Gaussian and large peak pressures occur. These large peak pressures are often the main cause of structural failures. The non-Gaussian characteristics of the surface

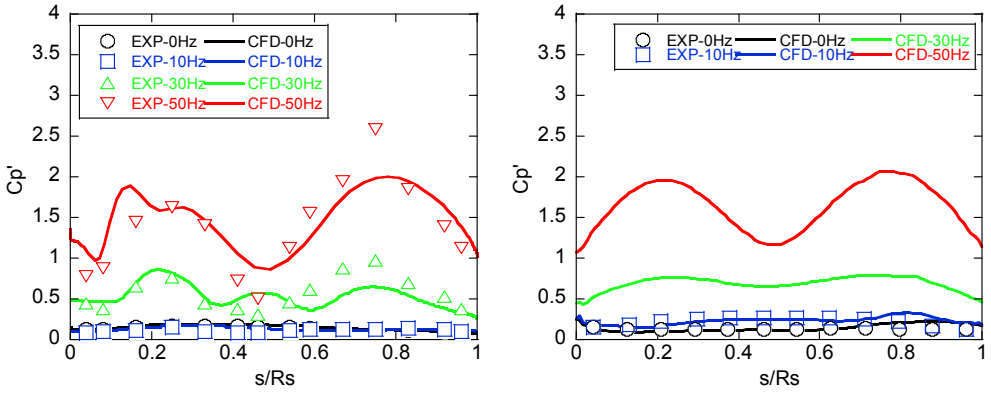

Fig. 12. Fluctuating pressure coefficients of roofs with different vibration frequencies.

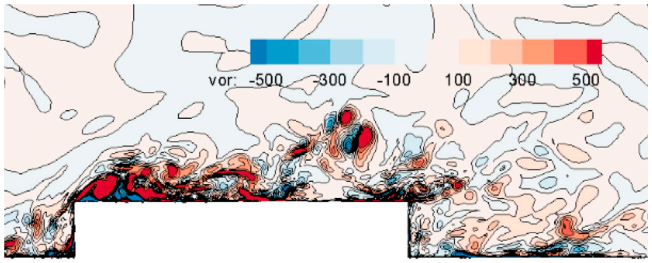

(a) φ=0

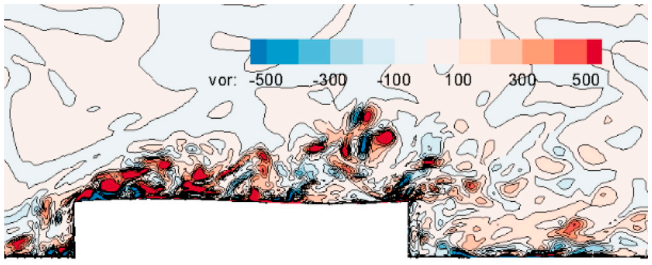

(b) φ=π/2

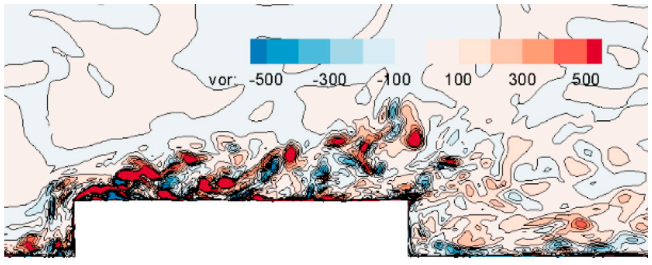

(c) φ=π

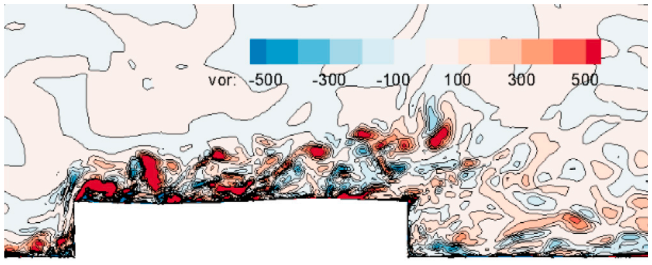

(d) φ=3π/2

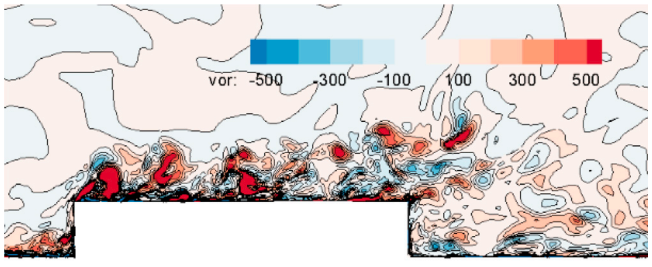

(e) φ=2π

Fig. 13. Transient vorticity contours around flat roof with different phases.

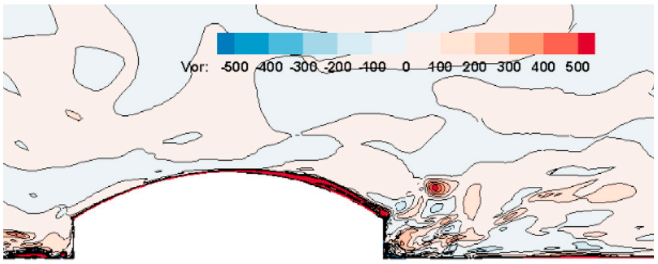

(a) φ=0

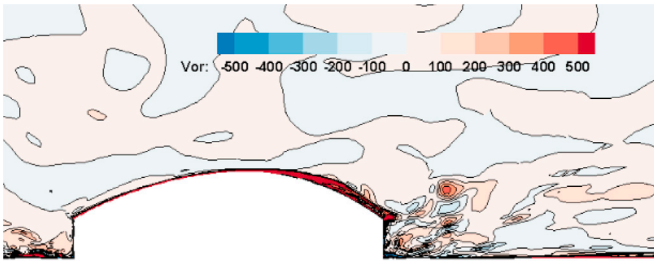

(b) φ=π/2

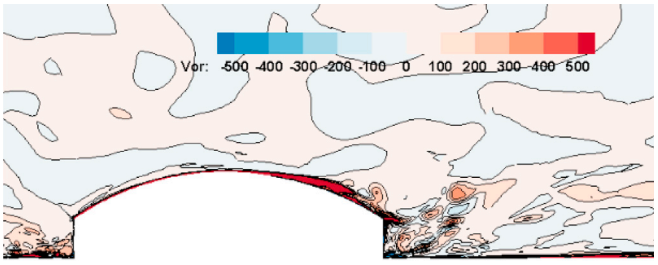

(c) φ=π

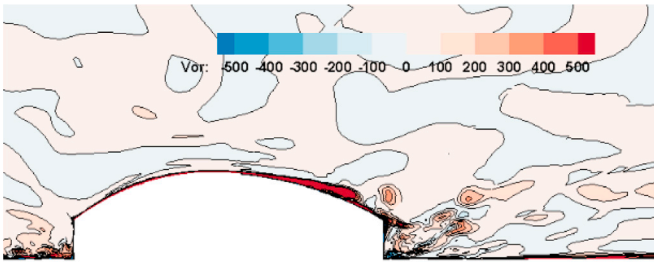

(d) φ=3π/2

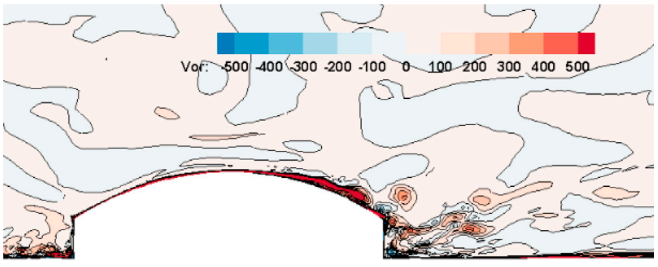

(e) φ=2π

Fig. 14. Transient vorticity contours around curved roof with different phases.

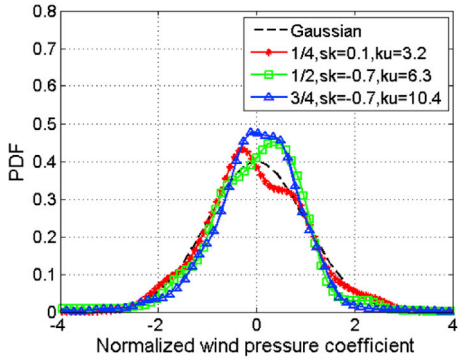

(a) Flat roof (f_m=0Hz)

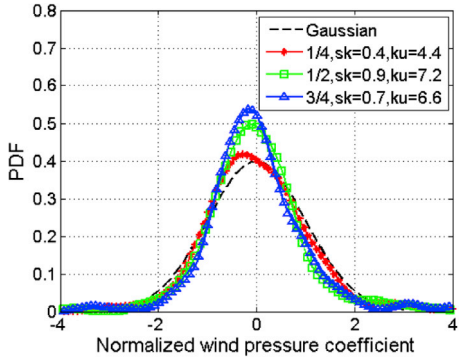

(b) Flat roof (f_m=10Hz)

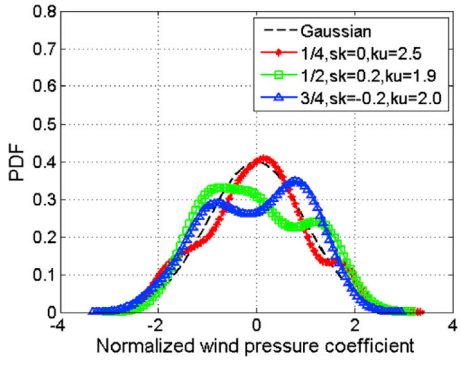

(c) Flat roof (f_m=30Hz)

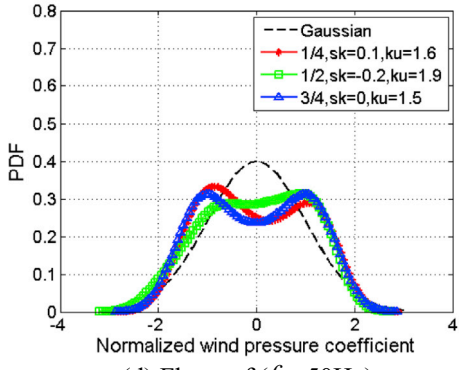

(d) Flat roof (f_m=50Hz)

Fig. 15. PDFs of wind pressure coefficient of flat roof with different vibration frequencies.

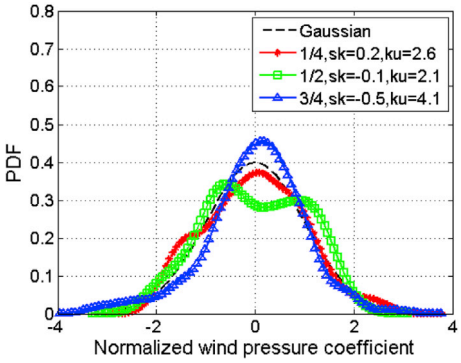

(a) Curved roof (f_m=0Hz)

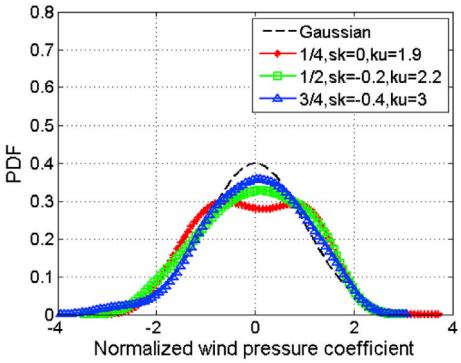

(b) Curved roof (f_m=10Hz)

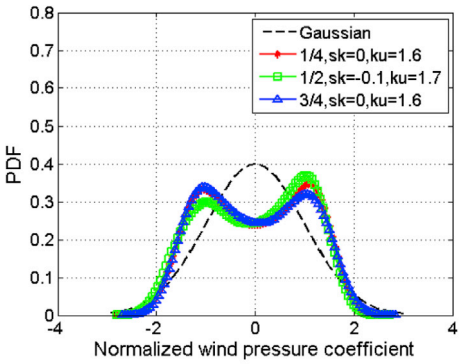

(c) Curved roof (f_m=30Hz)

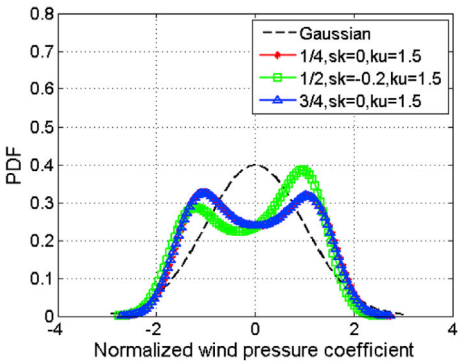

(d) Curved roof (f_m=50Hz)

Fig. 16. PDFs of wind pressure coefficient of curved roof with different vibration frequencies.

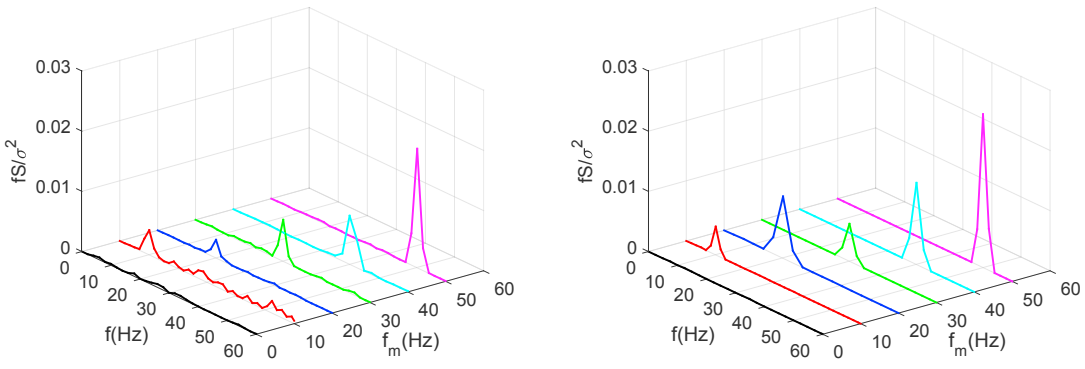

(a) Flat roof (b) Curved roof

Fig. 17. PSDs of wind pressure coefficient.

wind pressures on long-span roofs considering the vibrating effect are studied in this section.

Skewness and kurtosis of the probability density function (PDF) are generally used to describe the non-Gaussian characteristics of wind pressure, which are defined as

$$C_{pi,sk} = E\left[\left(\frac{C_{pi}(t) - C_{pi,mean}}{C_{pi,rms}}\right)^3\right] \tag{17}$$

$$C_{pi,ku} = E\left[\left(\frac{C_{pi}(t) - C_{pi,mean}}{C_{pi,rms}}\right)^4\right] \tag{18}$$

where subscript *i* is the identifier of point on the roof; *sk* and *ku* stand for skewness and kurtosis respectively; *mean* and *rms* stand for the mean and standard deviation of variables. *E* denotes the expectation value.

Based on the numerical time history of wind pressures on flat and curved roofs, their PDFs at points with maximum vibration amplitude ($s/R_s = 1/4$, $3/4$) and the roof center point ($s/R_s = 1/2$) are shown in Figs. 15 and 16. The skewness and kurtosis of each measure point are shown in the labels. A standard Gaussian distribution curve with null mean and unit variance is also plotted for comparison.

The PDF of the fluctuating wind pressure on rigid roof is close to the Gaussian distribution as shown in Fig. 15(a) and Fig. 16(a). For the vibrating roofs, the PDF changes from single peak distribution to double peak distribution with increasing excitation frequency (Fig. 15(b, c, d) and 16(b, c, d)). The PDF with double peaks is similar to the PDF of the excited sinusoidal displacement of the roof. This indicates that with increasing vibration frequency, the correlation between the wind load on roof and the roof displacement is strengthened. With increasing vibration frequency, the skewness *sk* tends to be zero, same as the value of Gaussian distribution. This may be due to the fact that the fluctuating pressure on the vibrating roof mainly depends on vibration, and it fluctuates symmetrically and synchronously with vibration. However, the kurtosis *ku* decreases gradually to 1.5 with increasing vibration frequency, which is quite lower than the Gaussian value as 3.0. It should be mentioned that when the PDF has one peak, its *ku* is always larger than the Gaussian value of 3.0 if the peak of PDF is higher than the Gaussian one, as shown in Fig. 15(a) and (b). However, this character cannot be found for the PDF with two peaks. Similar results are shown in the research of Chen (2013).

The PDF function of curved roof changes to double peak distribution at a lower excitation frequency than the flat roof. This may be due to the fact that the effect of vibration is dominating only in higher vibration frequency for flat roof, while the influence of separated flow on the fluctuating wind pressure is smaller for the curved roof and the vibration effect is more easily to dominate. The PDF of wind pressure shows obvious non-Gaussian characteristics when the vibrating condition is taken into account. Therefore, the peak value of wind pressure on flexible roofs could be estimated using non-Gaussian estimation methods, e.g. the translation process method (Yang and Tian, 2015; Huang et al., 2016; Liu et al., 2017).

4.4. Power spectral density of wind pressure

The fluctuating wind pressure spectrum is always used to measure the contribution of fluctuating wind pressure components in different frequency bands. For the rigid roof, the energy of fluctuating wind pressure mainly comes from buffeting components, e.g. the components induced by the turbulence of inflow and wake. However, the component of vibration-induced force should be added upon the buffeting components for the flexible roof, which is studied in this section.

The dimensionless wind pressure spectrum $f \cdot S(f)/\sigma^2$ at a typical position ($s/R_s = 1/4$) on the flat and curved roofs for different vibration frequencies are shown in Fig. 17, where $S(f)$ is the function of Power Spectral Density (PSD) and σ^2 is the variance of fluctuating wind pressure. The spectra of buffeting components can be found on the rigid roofs ($f_m = 0$ Hz), which are relatively smooth, while the spectra on the vibrating roofs include peaks corresponding to the excitation frequencies. These peaks are quite larger than the spectral values on the rigid roofs, and they roughly increase with the excitation frequency. This proves that the vibration-induced components provides much more energy to the fluctuating pressure than the buffeting force components. The increase of the spectral peak value with excitation frequency is due to the increasing energy input from the roof vibration. That is why the fluctuating pressure and its PDF primarily depend on vibration frequency, as shown in Figs. 12, 15 and 16. The characteristics of wind pressure spectrum obtained here are in agreement with experimental results (Ohkuma and Marukawa, 1990).

5. Unsteady aerodynamic characteristics

5.1. Unsteady aerodynamic force coefficients

The wind load on the long-span roof changes significantly with vibration as discussed above. The component of vibration induced wind load is called the unsteady aerodynamic force or self-excited aero-elastic force (Kareem and Gurley, 1996). This force is sometimes the controlling factor on structural dynamic instability for flexible structures like long-span roofs. In view of the complexity of the coupling between wind and structure, a simplified dynamic equation for multiple-degree-of-freedom system under fluctuating wind load has been proposed (Katagiri et al., 2001) as

$$M_S\ddot{z} + C_S\dot{z} + K_S z = F_T(t) + F_W(t) + F_A(t, z, \dot{z}, \ddot{z}) \tag{19}$$

The terms on the left-hand-side stand for structural inertia force,

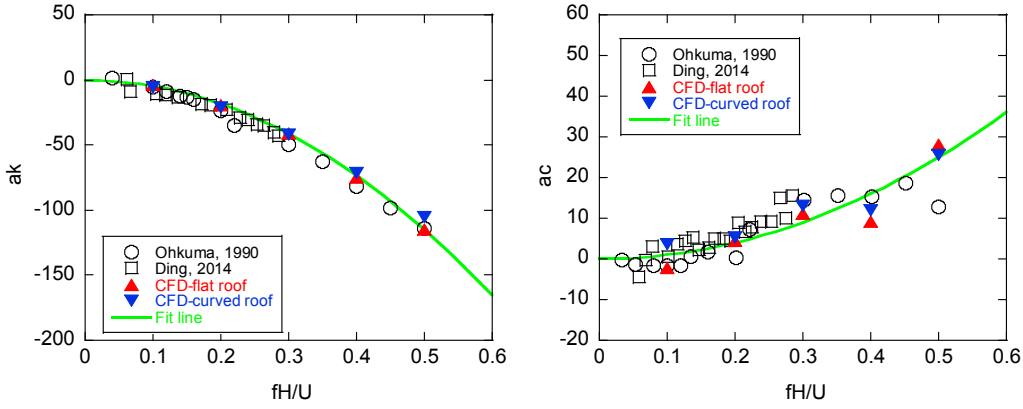

(a) Aerodynamic stiffness coefficients (b) Aerodynamic damping coefficients

Fig. 18. Unsteady aerodynamic coefficients.

damping force and stiffness force respectively. The terms on the right-hand-side are forces due to the turbulent inflow, the wake instability, and the self-excited forces, denoted as F_T, F_W and F_A respectively. It is noted that the self-excited force F_A is a function of time, displacement, velocity and acceleration.

The self-excited force F_A can be separated into two terms because of the orthogonality of displacement and velocity. The force related with displacement z and acceleration $\ddot{z}$ is called the in-phase aerodynamic force A. The force related with velocity $\dot{z}$ is called the out-of-phase aerodynamic force A^* and they are related as

$$F_A(t,z,\dot{z},\ddot{z}) = A(t,z,\ddot{z}) + A^*(t,\dot{z}) \tag{20}$$

If the structure vibrates in small amplitude, the in-phase and out-of-phase aerodynamic forces may be assumed as linear functions of displacement and its derivative. The two terms on the right-hand-side of Eq. (20) can thus be expressed as

$$A(t,z,\ddot{z}) = -K_a z \tag{21}$$

$$A^*(t,\dot{z}) = -C_a \dot{z} \tag{22}$$

where K_a and C_a are the relation coefficients between unsteady aerodynamic force and the displacement and velocity respectively. K_a and C_a are called the aerodynamic stiffness and damping respectively as they lead to a change in the equivalent stiffness and damping of the system. Thus the dynamic equation of motion in Eq. (19) can be written as:

$$M_S\ddot{z} + (C_S + C_a)\dot{z} + (K_S + K_a)z = F_T(t) + F_W(t) \tag{23}$$

The discussions above are based on two assumptions: (a) The influence of vibration on the buffeting force is ignored; and (b) the harmonic components of unsteady aerodynamic force apart from that at the vibration frequency are ignored. These approximations are acceptable in engineering practices. Another point worth mentioning is that since the displacement z and the acceleration $\ddot{z}$ share the same phase, the aerodynamic stiffness and mass effects cannot be separated in this method.

The in-phase aerodynamic coefficient of the hanging roof is generally described as the aerodynamic mass, and the aerodynamic stiffness is generally referred to that for the closed roof (Yang et al., 2010). The fluid and structure can be treated as parts of the same system using this simplified dynamic equation, and the influence of unsteady aerodynamic force is equivalent to that due to a change of system dynamic parameters. Once the unsteady aerodynamic terms have been determined, the interaction effect between wind and structure can be solved as a general stochastic vibration problem utilizing existing random vibration theories.

Non-dimensional unsteady aerodynamic force coefficients are always used to represent the characteristics of unsteady aerodynamic force and to calculate the dynamic response in the frequency domain. The aerodynamic stiffness coefficient a_K and aerodynamic damping coefficient a_C are defined by Eqs. (24) and (25) (Daw and Davenport, 1989) as

$$a_K = -\frac{1}{z_0/L}\frac{2}{T}\int_0^T \frac{F(t)}{q_H A_s}\frac{z(t)}{z_0}dt \tag{24}$$

$$a_C = -\frac{1}{z_0/L}\frac{2}{T}\int_0^T \frac{F(t)}{q_H A_s}\frac{\dot{z}(t)}{\dot{z}_0}dt \tag{25}$$

where A_s is the area of roof; T is the period of forced vibration and $F(t)$ is the generalized wind force. It is worth noting that the signs of the unsteady aerodynamic coefficients defined in Eqs. (24) and (25) are same with the aerodynamic stiffness and damping, which is consistent with the definition in Daw and Davenport (1989) but opposite the ones in Ohkuma and Marukawa (1990), Kawai et al. (1999) and Ding et al. (2014).

The aerodynamic stiffness and damping coefficients are obtained using the wind pressure time history at all points on the roof. Numerical results of the flat roof and curved roof are compared with experimental results (Ohkuma and Marukawa, 1990; Ding et al., 2014), as shown in Fig. 18. In this range of frequencies the aerodynamic stiffness coefficient is negative and the aerodynamic damping coefficient is positive. Both of the values increase in magnitude with the reduced frequency. It can be seen that the unsteady aerodynamic coefficients of different roof shapes almost coincide, indicating that the unsteady aerodynamic coefficients mainly depend on the reduced vibration frequency in this range of frequency and amplitude, and they are independent with the shape of roof. It should be mentioned that the sign of a_K and a_C is changed when the previous results (Ohkuma and Marukawa, 1990; Ding et al., 2014) are plotted in Fig. 18 together with the present results.

Since the aerodynamic stiffness and damping coefficients mainly depend on the reduced frequency, they can be curve-fitted as functions of the reduced frequency as shown in Fig. 18. The fitted formulas are

$$a_k = -460f^* = -460 \times \left(\frac{fH}{U}\right)^2 \tag{26}$$

$$a_c = 100f^{*2} = 100 \times \left(\frac{fH}{U}\right)^2 \tag{27}$$

where $f^* = fH/U$ is the reduced frequency. It should be noticed that the unsteady aerodynamic coefficients may also be influenced by the vibration amplitude for large amplitude cases. However, they are independent of amplitude when $x_0/H \leq 0.1$ as shown in the experimental results (Ohkuma and Marukawa, 1990).

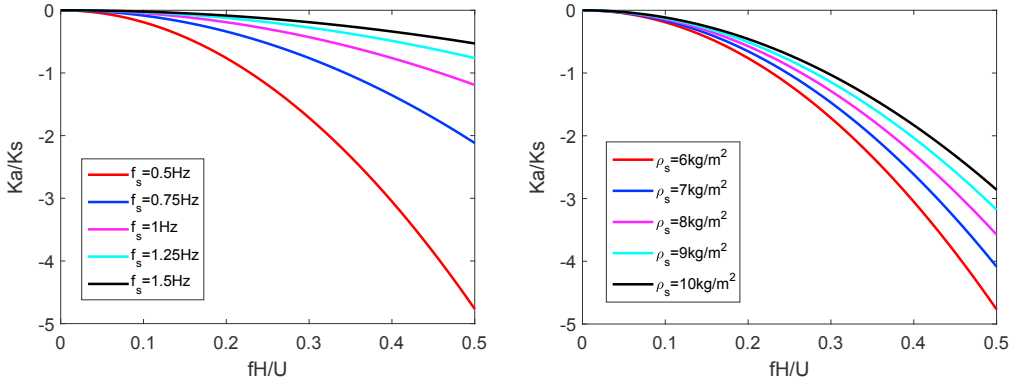

(a) Effect of roof natural frequency (b) Effect of roof density

Fig. 19. Aerodynamic stiffness ratios.

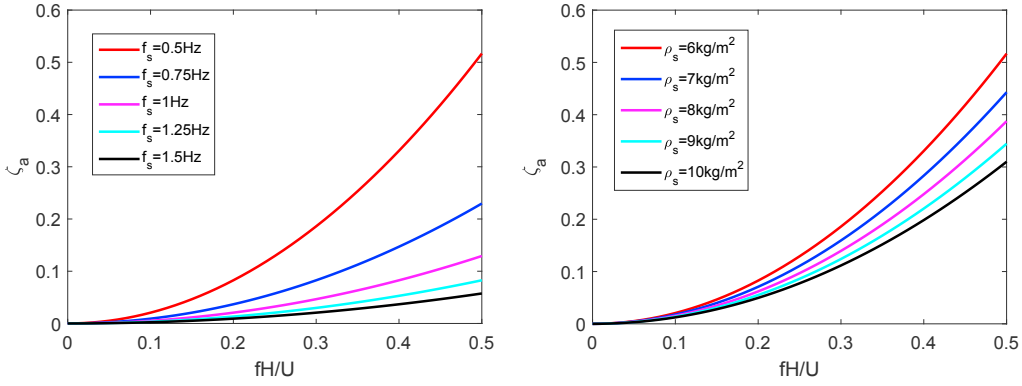

(a) Effect of roof natural frequency (b) Effect of roof density

Fig. 20. Aerodynamic damping ratios.

5.2. Prediction of dynamic response

The dynamic responses of long-span roofs under the effects of unsteady aerodynamic forces are studied in this section. The dynamic response of the structure is calculated using the generalized force spectrum and the mechanical admittance function, i.e. the transfer function between the wind pressure spectrum and the dynamic response spectrum, as shown in Eqs. (28) and (29) (Daw and Davenport, 1989):

$$\sigma_x^2 = \frac{1}{K_s^2}\int_0^\infty S_F(f)|H(f)|^2 df \tag{28}$$

$$|H(f)|^2 = \frac{1}{\left[1-\left(\frac{f}{f_s}\right)^2+\frac{K_a(f)}{K_s}\right]^2+4(\zeta_s+\zeta_a(f))^2\left(\frac{f}{f_s}\right)^2} \tag{29}$$

where, σ_x^2 is the variance of the dynamic response. K and ζ denote the stiffness and damping respectively. $S_F(f)$ is the spectrum of generalized force. $H(f)$ is the mechanical admittance, which is a function of frequency ratio, stiffness ratio and damping ratio. The subscripts a and s refer to aerodynamic coefficients and structural coefficients respectively. The stiffness ratio and damping ratio can be obtained from the unsteady aerodynamic coefficients as

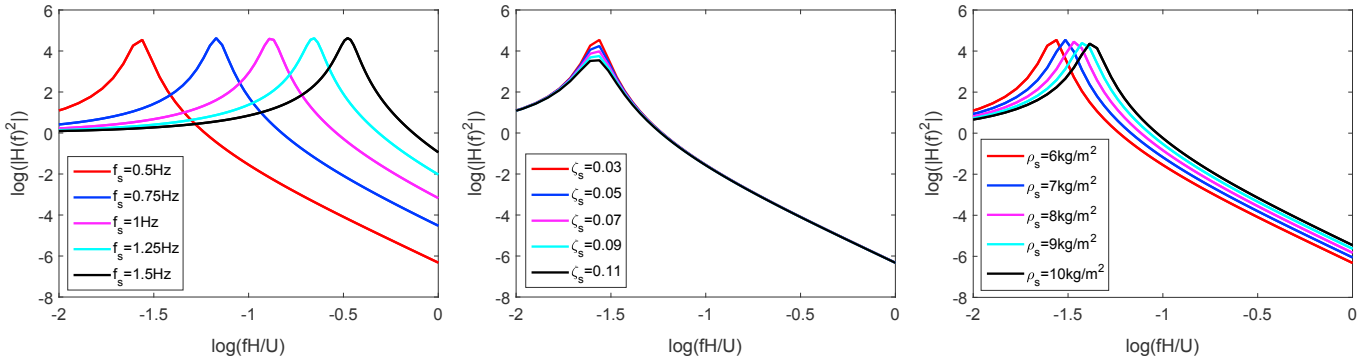

(a) Effect of roof natural frequency (b) Effect of roof damping ratio (c) Effect of roof density

Fig. 21. Mechanical admittance functions.

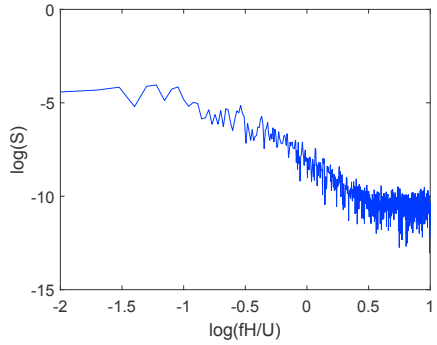

Fig. 22. Spectrum of generalized wind load coefficient.

$$\frac{K_a(f)}{K_s} = \frac{1}{8\pi^2}\frac{\rho_a}{\rho_s}\left(\frac{U_H}{f_s H}\right)^2 \frac{H}{L} a_K(f) \tag{30}$$

$$\zeta_a(f) = \frac{1}{16\pi^2}\frac{\rho_a}{\rho_s}\left(\frac{U_H}{f_s H}\right)^2 \frac{H}{L} a_C(f) \tag{31}$$

where the unsteady aerodynamic coefficients a_K and a_C are obtained by Eqs. (26) and (27).

The influence of unsteady aerodynamic forces on the dynamic response of a real-scale structure is studied here. The span and height of the long-span flexible roof are assumed to be 100 m and 20 m respectively. Its natural frequency f_s, damping ratio ζ and density ρ have the ranges of 0.5 Hz–1.5 Hz, 3%–11% and 6 kg/m^2 to 10 kg/m^2 respectively. To investigate the influence of each structural parameters, control variable method is used. In the baseline model, f_s is set as 0.5 Hz, ζ as 3% and ρ as 6 kg/m^2. For each case only one parameter changes and the others are kept as constants as the baseline model. The structural dynamic responses obtained are discussed below.

Firstly, the effects of roof parameters on stiffness ratios and damping ratios are obtained as shown in Figs. 19 and 20. It can be seen that the aerodynamic stiffness ratio is negative and decrease with the reduced frequency, resulting in a reduction of total stiffness. Meanwhile the aerodynamic damping ratio will increase the total damping. When the natural frequency or material density of roof increases, both of the effects of aerodynamic stiffness and damping are reduced.

The mechanical admittance function of the system can be calculated based on the results of the stiffness and damping ratio, as shown in Fig. 21. It is noted that the peak of mechanical admittance function remains relatively constant with increasing structural natural frequency, while the normalized frequency at the peak value increases significantly. With increasing damping of the structure, the peak of mechanical admittance decreases while the peak position remains unchanged. In addition, the peak of function reduces slightly when the mass of roof increases, and the normalized frequency at the peak value increases slightly at the same time.

The spectrum of generalized wind load on the roof from numerical simulation is shown in Fig. 22. According to the wind load spectrum and the curves of mechanical admittance, the variance of generalized displacements can be calculated, and the results with and without considering unsteady aerodynamic coefficient are compared, as shown in Fig. 23.

The dynamic response is noted under-estimated without considering the unsteady aerodynamic force on the roof with smaller stiffness ($f_s = 0.5$ Hz) as shown in Fig. 23(a). For the more rigid roofs, e.g. $f_s > 0.75$ Hz, the dynamic responses are similar no matter unsteady aerodynamic forces are considered or not, which means the unsteady aerodynamic effect can be ignored for rigid roofs. Then the effect of roof damping ratio and density are tested base on the flexible roof ($f_s = 0.5$ Hz). The results in Fig. 23(b) and (c) show that when the structural damping or density becomes larger, the dynamic response of the flexible roof is always under-estimated without considering unsteady aerodynamic forces, which indicates stiffness rather than damping or mass plays a more important role in this case.

6. Conclusions

Long-span roofs with different shapes under forced excitation are simulated based on the LES turbulence model. The wind pressure and unsteady aerodynamic force coefficients are predicted, and their characteristics are investigated based on numerical flow patterns. The dynamic response is evaluated with consideration of the unsteady aerodynamic forces. The following main conclusions are drawn:

(1) The mean wind pressure coefficients mainly depend on the position of flow separation and vortex shedding, and therefore the difference is obvious for different shapes of roofs. The vibration of structure, however, has little effect on the mean wind pressure. The fluctuating pressure contains not only the components of inflow and wake effects but also the roof vibration-induced component, which becomes dominant when the roof vibrates at higher excitation frequency. The distribution of fluctuating pressure coefficient at higher vibration frequency depends on the vibration mode as a result. The maximum value of the fluctuating pressure coefficient increases with vibration frequency. The symmetric distribution of fluctuating pressure coefficients is influenced by the position of flow separation and vortex shedding. It is only symmetric when the vortices shed near the trailing edge of roof.

(2) The PDF of the fluctuating wind pressure from the vibrating roof shows non-Gaussian characteristics. It changes from single peak distribution to double peak distribution with an increase of the excitation frequency, indicating a strengthening of the correlation

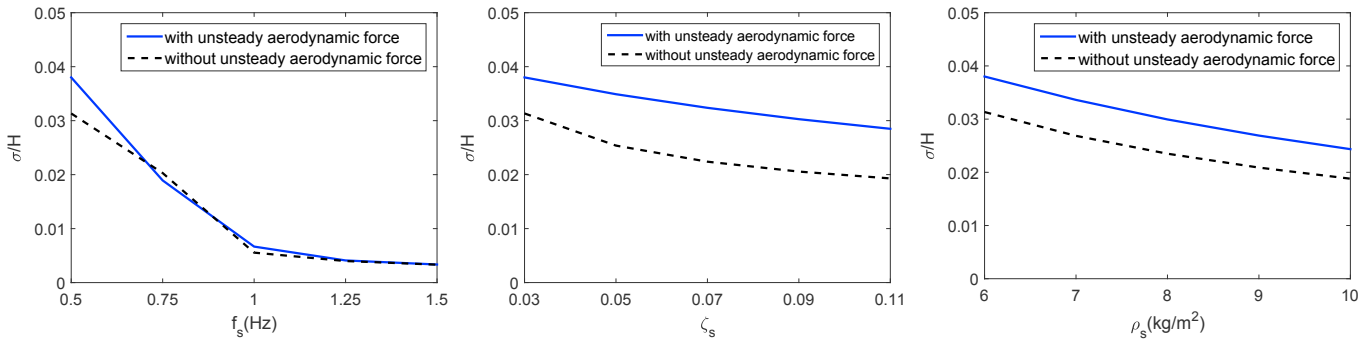

(a) Effect of roof natural frequency (b) Effect of roof damping ratio (c) Effect of roof density

Fig. 23. Variations of standard deviation of generalized displacement with structural parameters.

between the wind load and the vibration displacement. The PSDs of the fluctuating wind pressure exhibit peaks corresponding to the vibration frequencies, indicating vibration is the main source of energy of the fluctuating wind pressure on the roof.

(3) The unsteady aerodynamic coefficients mainly depend on the reduced vibration frequency, and they are insensitive to the roof shape. The unsteady aerodynamic effect lead to a decrease of total stiffness and an increase of total damping of the structure. The dynamic response of structures will be under-estimated without considering the unsteady aerodynamic forces, especially for flexible structures. Stiffness rather than damping or mass plays a more important role in this case.

It is noted that the results presented in this paper are preliminary based on the first asymmetric vibration mode of the structure. Multiple vibration modes should be considered for real structures and more simulations are needed to study the behavior with higher vibration modes. The predicted dynamic responses should be compared with results from aero-elastic experiments in the further study.

Acknowledgements

This study has been partially supported by 111 Project (B13002, B18062), National Natural Science Foundation (51720105005) and 1000 Foreign Talents Plan (WQ20131100144) of the Chinese Government. The comments and work by Prof. Siu-seong Law in improving the English of this paper are fully acknowledged. We would also like to acknowledge Prof. Xingzhong Chen for his helpful comments on this work.

References

ANSYS Inc, 2015. ANSYS FLUENT 16.2 User's Guide.
Chen, X., 2013. Estimation of stochastic crosswind response of wind-excited tall buildings with nonlinear aerodynamic damping. Eng. Struct. 56, 766–778.
Chen, Z., 2015. Investigation of aeroelastic instability mechanism of tensioned membrane structures. Harbin Institute of Technology (in Chinese).
Chen, Z., Wu, Y., Sun, X., 2015. Research on aeroelastic instability mechanism of closed-type one-way tensioned membrane. J. Build. Struct. 36, 12–19 (in Chinese).
Daw, D.J., Davenport, A.G., 1989. Aerodynamic damping and stiffness of a semi-circular roof in turbulent wind. J. Wind Eng. Ind. Aerod. 32, 83–92.
Ding, W., Uematsu, Y., Nakamura, M., Tanaka, S., 2014. Unsteady aerodynamic forces on a vibrating long-span curved roof. Wind Struct. 19, 649–663.
Ferziger, J., Peric, M., 2002. Computational Method for Fluid Dynamics, third ed. Springer, Berlin.
Hirsch, C., 2007. Numerical Computation of Internal and External Flows: the Fundamentals of Computational Fluid Dynamics. Butterworth-Heinemann.
Huang, G., Luo, Y., Gurley, K.R., Ding, J., 2016. Revisiting moment-based characterization for wind pressures. J. Wind Eng. Ind. Aerod. 151, 158–168.
Kareem, A., Gurley, K., 1996. Damping in structures: its evaluation and treatment of uncertainty. J. Wind Eng. Ind. Aerod. 59, 131–157.
Katagiri, J., Ohkuma, T., Marikawa, H., 2001. Motion-induced wind loads acting on rectangular high-rise buildings with side ratio of 2. J. Wind Eng. Ind. Aerod. 89, 1421–1432.
Kawai, H., Yoshie, R., Wei, R., Shimura, M., 1999. Wind-induced response of a large cantilevered roof. J. Wind Eng. Ind. Aerod. 83, 263–275.
Kimoto, E., Kawamura, S., 1983. Aerodynamic behavior of one-way type hanging roof. J. Wind Eng. Ind. Aerod. 13, 395–405.
Kunieda, H., 1975. Flutter of hanging roofs and curved membrane roofs. Int. J. Solid Struct. 11, 477–492.
Liu, M., Chen, X., Yang, Q., 2017. Estimation of peak factor of non-Gaussian wind pressures by improved moment-based Hermite model. J. Eng. Mech. 143 (7), 06017006.
Ma, X., Karamanos, G.S., Karniadakis, G.E., 2000. Dynamics and low-dimensionality of a turbulent near wake. J. Fluid Mech. 410, 29–65.
Miyake, A., Yoshimura, T., Makino, M., 1992. Aerodynamic instability of suspended roof models. J. Wind Eng. Ind. Aerod. 42, 1471–1482.
Matsumoto, T., 1990. Self-excited oscillation of a pretensioned cable roof with single curvature in smooth flow. J. Wind Eng. Ind. Aerod. 34, 304–318.
Ohkuma, T., Marukawa, H., 1990. Mechanism of aeroelastically unstable vibration of long span roof. J. Wind Eng. 42, 35–42 (in Japanese).
Oka, S., Ishihara, T., 2009. Numerical study of aerodynamic characteristics of a square prism in a uniform flow. J. Wind Eng. Ind. Aerod. 97, 548–559.
Sarwar, M.W., Ishihara, T., 2010. Numerical study on suppression of vortex-induced vibrations of box girder bridge section by aerodynamic countermeasures. J. Wind Eng. Ind. Aerod. 98, 701–711.
Sharekh, M.S.A., Pathak, S.K., 2000. Turbulent boundary layer over symmetric bodies with rigid and flexible surface. J. Eng. Mech. 126, 422–431.
Shen, S., Wu, Y., 2002. Overview of wind-induced response for long-span tension structures. J. Tongji Univ. 30, 533–538 (in Chinese).
Smagorinsky, J., 1963. General circulation experiments with the primitive equations. I. The basic experiment. Mon. Weather Rev. 91, 99–164.
Tamura, Y., Kareem, A., 2013. Advanced Structural Wind Engineering. Springer Science and Business Media.
Yang, Q., Liu, R., 2005. On aerodynamic stability of membrane structures. Int. J. Space Struct. 20, 181–188.
Yang, Q., Tian, Y., 2015. A model of probability density function of non-Gaussian wind pressure with multiple samples. J. Wind Eng. Ind. Aerod. 140, 67–78.
Yang, Q., Wu, Y., Zhu, W.L., 2010. Experimental study on interaction between membrane structures and wind environment. Earthq. Eng. Eng. Vib. 9, 523–532.